RESEARCH ARTICLE

Key Points:
- Poleward moving throat auroras show brightening followed by dimming
- Throat aurora brightening is sometimes a precursor of PMAF
- The throat aurora brightening and dimming are likely on open and closed field lines, respectively

Supporting Information:
- Supporting Information S1
- Movie S1
- Movie S2

Correspondence to:
X.-C. Chen,
xiangcai.chen@unis.no

Dynamic properties of throat aurora revealed by simultaneous ground and satellite observations

X.-C. Chen[1,2,3] (iD), D.-S. Han[4] (iD), D. A. Lorentzen[1,2] (iD), K. Oksavik[1,2] (iD), J. I. Moen[1,3], and L. J. Baddeley[1,2] (iD)

[1]Department of Arctic Geophysics, University Centre in Svalbard, Longyearbyen, Norway, [2]Birkeland Centre for Space Science, Department of Physics and Technology, University of Bergen, Bergen, Norway, [3]Department of Physics, University of Oslo, Oslo, Norway, [4]SOA Key Laboratory for Polar Science, Polar Research Institute of China, Shanghai, China

Abstract Throat aurora is defined as south-north aligned auroral arcs equatorward of the dayside cusp aurora and was suggested to be the results of cold magnetospheric plasma interaction with magnetopause reconnection, but its observational properties have not yet been well established. In this paper we carefully examine a sequence of throat auroras observed over Svalbard on 27 December 2003. Observations from 630.0 nm [OI] show that poleward moving throat auroras frequently show brightening followed by dimming in auroral intensity, and sometimes, the brightening throat aurora is a precursor of poleward moving auroral forms. Simultaneous all-sky images and HF radar backscatter observations along geomagnetic meridian show that the throat aurora brightening is drifting with ionospheric $E \times B$ convection and is colocated with enhanced spectral width poleward of the convection reversal boundary (CRB), while its dimming tends to be in the vicinity of the CRB. This leads us to propose that the throat aurora brightening and dimming may be on the open and closed field lines, respectively. Particle data from NOAA 16 confirm that the dimming throat aurora is associated with precipitation of magnetosheath-like particles mixed with magnetospheric ions (>30 keV), which is characteristic of the low-latitude boundary layer. For particle data from Defense Meteorological Satellite Program F16, we notice that the dimming throat aurora is associated with lower fluxes of magnetosheath-like electrons accompanied with magnetospheric electrons, which is most likely on closed field lines. The dynamic properties of throat aurora presented in this paper are thus important to understand its generation mechanisms.

1. Introduction

Auroras observed from the ground can be classified into discrete and diffuse auroras based on their morphological properties [e.g., *Sandholt et al.*, 1998]. The discrete auroras normally show structured forms, such as arcs, bands, and rays, and are generated by particle acceleration along magnetic field lines [e.g., *Li et al.*, 2013]. The diffuse aurora represents a region of relatively homogenous and weak luminosity at the equatorward edge of the auroral oval [e.g., *Lorentzen and Moen*, 2000; *Moen et al.*, 1998; *Sandholt et al.*, 1998] and is regarded as resulting from scattering of central plasma sheet (CPS) electrons into the loss cone by electron cyclotron harmonic waves [*Horne et al.*, 2003; *Liang et al.*, 2010; *Ni et al.*, 2011a] or whistler mode chorus waves [*Li et al.*, 2010; *Ni et al.*, 2011b; *Nishimura et al.*, 2013; *Thorne et al.*, 2010] on closed field lines. Diffuse auroras also sometimes show structured forms [*Han et al.*, 2015; *Lui et al.*, 1973; *Nishimura et al.*, 2013]. The structured diffuse aurora is suggested to result from cold plasma structures interacting with hot plasma sheet electrons [*Demekhov and Trakhtengerts*, 1994; *Liang et al.*, 2015].

Dayside auroras, especially around magnetic local noon (MLN), are believed to be the instant response to the interaction between the solar wind and the magnetosphere [e.g., *Sandholt et al.*, 1986]. Based on ground observations, *Sandholt et al.* [1998] classified the dayside auroras into five types depending on the orientation of the interplanetary magnetic field (IMF) and the magnetic local time (MLT), among which the type 1 and type 2 cusp auroras observed near MLN are believed to be due to low- and high-latitude reconnections for southward and northward IMFs, respectively. A central feature for the type 1 cusp aurora is the phenomenon of poleward moving auroral forms (PMAFs), which is an ionospheric manifestation of pulsed magnetopause reconnection [e.g., *Sandholt and Farrugia*, 2007]. *Sandholt et al.* [1998] noticed that the diffuse aurora can often be observed equatorward of the auroral oval from morning to MLN, and they called it type 3 aurora.

Recently, *Han et al.* [2015] carried out a systematic study of the type 3 aurora [*Sandholt et al.*, 1998] and found that the dayside diffuse auroras include both unstructured and structured forms. The structured ones often show stripy, patchy, and irregular forms and are predominantly occurring around MLN. The orientation of the stripy diffuse aurora was consistent with the ionospheric convection. When the stripy diffuse aurora extends poleward toward the persistent east-west (E-W) aligned auroral oval, a south-north (S-N) oriented discrete auroral arc is often observed equatorward of the auroral oval. The S-N aligned arc was called throat aurora by *Han et al.* [2015] because it occurs only in the ionospheric convection throat region near MLN. Observational properties and the factors affecting generation of throat aurora have been proposed by *Han et al.* [2017]. It was suggested that the stripy diffuse aurora is magnetically conjugated to a wedge-like cold plasma structure in the dayside outer magnetosphere, and the throat aurora is generated when the cold plasma flows into the magnetopause reconnection site [*Han et al.*, 2015, 2016]. Interaction of cold magnetospheric plasma with the dayside magnetic reconnection region has attracted much attention in recent years [*Borovsky and Denton*, 2006; *Fuselier et al.*, 2016; *Walsh et al.*, 2014], but it is still poorly understood. The studies of *Han et al.* [2015, 2016] imply that continuous ground-based observations of throat aurora may provide important information on the interaction of cold magnetospheric plasma with the magnetopause reconnection region. Although *Han et al.* [2016] suggested that the throat aurora is the ionospheric signature of magnetosheath particles penetrating into the magnetosphere along open field lines, the dynamic properties of throat aurora have not yet been investigated in great detail.

In this paper we will use multiple satellite and ground-based instrumentation to examine a sequence of throat auroras showing a brightening followed by a dimming feature. Observations of the throat aurora include HF radar backscatter, optical emission intensity, and satellite particle observations. An intimate relationship between the brightening of the throat aurora and PMAFs will also be studied. The dynamic properties of the throat aurora are critical for understanding how it relates to the solar wind/magnetosphere coupling when the cold magnetospheric plasma interacts with the dayside reconnection region.

2. Data and Instrumentation

2.1. All-Sky Imager

An auroral observation system was set up at the Yellow River Station (YRS) at Ny-Ålesund (geographic: 78.92°N, 11.93°E; magnetic latitude: 76.24° MLAT) in Svalbard in 2003. Three all-sky imagers simultaneously record the wavelengths at 427.8 (blue line), 557.7 (green line), and 630.0 (red line) nm, respectively. Each image is captured by a CCD of 512×512 pixels every 10 s, including 7 s exposure time and 3 s readout time. The recorded absolute Rayleigh intensity was initially calibrated at the National Institute of Polar Research, Japan [*Hu et al.*, 2009]. The discrete aurora is simultaneously monitored in both the red and green lines which originate at different altitudes, but the diffuse aurora is predominantly observed in the green line. Each image is cut at 80° zenith angle, before it is projected to the assumed emission heights of 200 (red) and 150 (green) km (we will discuss this choice below) and transformed into Altitude Adjusted Corrected Geomagnetic Coordinates (AACGM). The MLT at YRS is approximately equal to universal time (UT) plus 3 h.

2.2. Super Dual Auroral Radar Network Finland Radar

The Finland HF radar forms part of the Super Dual Auroral Radar Network (SuperDARN) array and is located at Hankasalmi (62.3°N, 26.6°E). It is ideally situated for making observations of the cusp ionosphere over Svalbard [e.g., *Moen et al.*, 2001, 2002]. When the refracted radar wave vector is nearly orthogonal to the local magnetic field, and field-aligned ionospheric irregularities satisfy the Bragg scale, maximum backscatter power is obtained. By transmitting a seven-pulse sequence and processing the received signals, the ionospheric plasma Doppler spectral power, line-of-sight velocity, and spectral width can be derived for each beam and range gate [*Greenwald et al.*, 1995].

On 27 December 2003 the radar was operating around 11.3 MHz using a dual scan mode (channels A and B). Channel A utilizes a 16-beam scan, with each beam separated by 3.24°, resulting in a 52° wide azimuthal scan starting from 12° west of geographic north, while channel B employed a single beam. Using a dwell time of 3 s, the radar scanned through beams 15 to 0 in descending order every 1 min. In this study only channel A data are used. With a distance to the first range gate of 180 km and 75 sampled range gates at each beam (each range gate is 45 km long), range gates 40–45 typically correspond to the location of Ny-Ålesund, depending on propagation conditions [e.g., *Chen et al.*, 2015, 2016; *Yeoman et al.*, 2008]. This is due to the
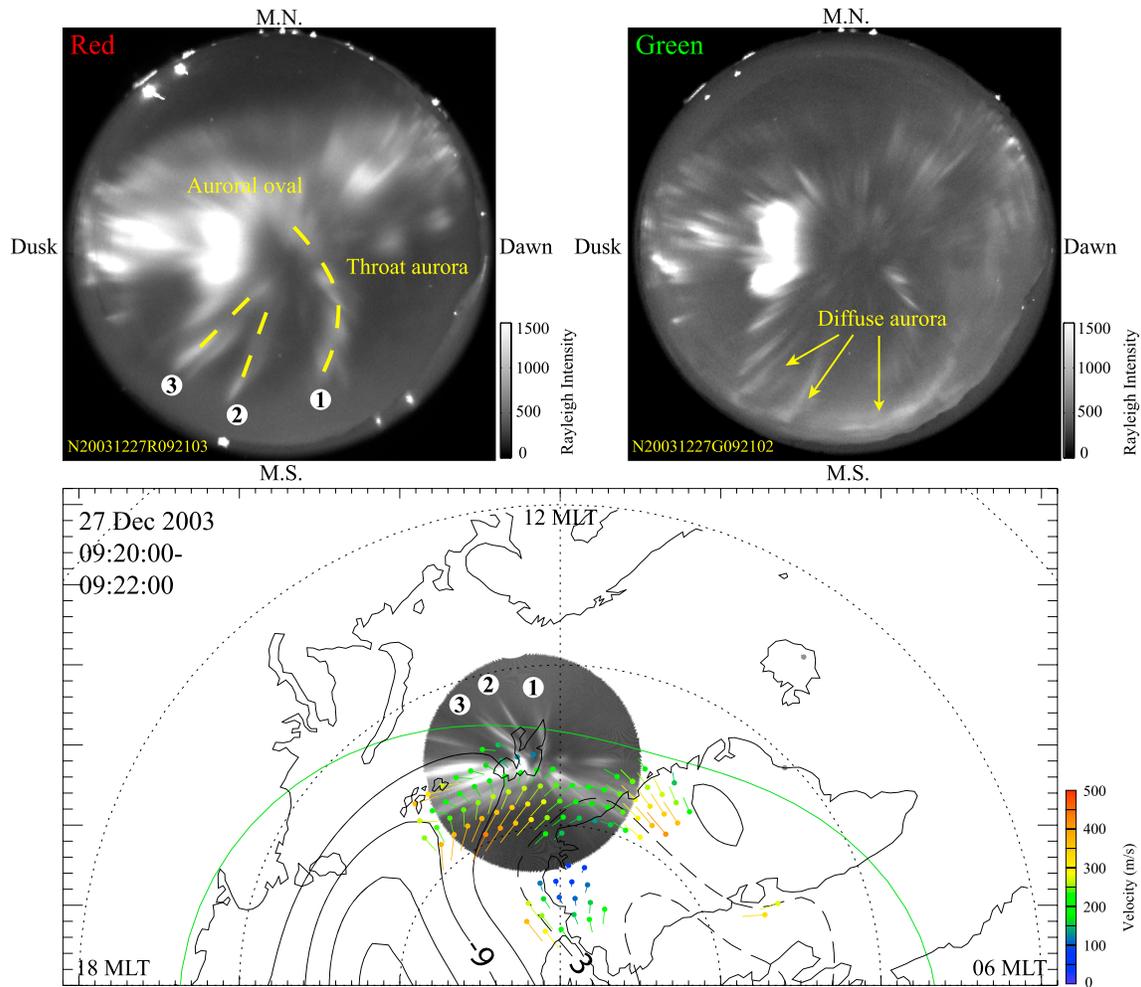
Figure 1. (top row) A snapshot of the throat aurora in the red and green lines observed by all-sky imagers. Magnetic north, south, west (dawn), and east (dusk) are marked on each image. (bottom) Simultaneous measurements of the dayside ionospheric plasma convection from SuperDARN in MLAT/MLT coordinates are presented (the Sun is to the top). The field of view of the red line aurora is overlaid, using an assumed emission altitude of 200 km and a cutoff at 80° zenith angle.

fact that SuperDARN currently employs a simple virtual model, i.e., assuming a fixed scattering height, to determine the location of its echoes, instead of a direct calculation of the ray path. A recent statistical observation [*Chen et al.*, 2016] of the SuperDARN Finland radar spectral width boundary, transferring from narrow to broad, showed that the location of radar echoes near Svalbard is, on average, overestimated by ~2° (~1°) latitude in the poleward direction during solar maxima (solar minima). This is consistent with the theoretical analysis of *Chisham et al.* [2008]. For the current study, we thus estimate the location of radar echoes over Ny-Ålesund to be around range gate 42.

2.3. Particle Data From NOAA 16

Data from the Space Environment Monitor (SEM-2) on board the polar-orbiting environmental satellites NOAA 16 spacecraft in 864 km altitude are used. The onboard Total Energy Detector (TED) monitors ion and electron energies in 16 channels ranging from 50 eV to 20 keV in two directions, both inside the loss cone (0° and 30° off zenith). The Medium Energy Proton and Electron Detector (MEPED) measures ion and electron energies above 30 keV at two directions, including one inside (10° off zenith) and one outside (80° off zenith) the loss cone. MEPED makes one measurement every 2 s, and TED makes one measurement every 8 s. For TED we use data from four energy channels (154–224, 688–1000, 2115–3075, and 6503–9457 eV). For MEPED we use fluxes of ions (30–80 keV) and electrons (>30, >100, and >300 keV) at angles of 10° and 80° to zenith. A more detailed description of the NOAA spacecraft and the SEM-2 instrumentation is provided by *Evans and Greer* [2000].

2.4. Particle Data From Defense Meteorological Satellite Program F16

The Defense Meteorological Satellite Program (DMSP) F16 spacecraft flies in a Sun-synchronous circular polar orbit at ~840 km altitude, where it records the fluxes of electrons and ions with energies from 30 eV to 30 keV, once per second, in 19 logarithmically spaced energy steps [*Hardy*, 1984]. Penetrating radiation at times produces a nearly constant background across the 19 energy channels, which can be detected by the Special Sensor J (5) particle detector and is removed.

2.5. Solar Wind and IMF Data

The upstream solar wind and IMF conditions are monitored by the Advanced Composition Explorer (ACE) satellite at the L1 Lagrange point. For this study, ACE was located around (240, −20, and 20) R_E in GSM coordinates. The solar wind and IMF data with 64 and 16 s resolution are presented from the solar wind experiment [*McComas et al.*, 1998] and the magnetometer instrument [*Smith et al.*, 1998].

3. Observation

A sequence of throat auroras entering the field of view of all-sky imager is observed between 09:00 and 09:40 UT (i.e., ~12:00–12:40 MLT) on 27 December 2003. Figure 1 shows a snapshot of the red and green line auroras observed at ~09:21 UT (top row), as well as the relative location and field of view (red line) of the YRS all-sky imager (bottom). Simultaneous measurements of ionospheric plasma convection derived from the SuperDARN map potential model [*Ruohoniemi and Baker*, 1998] are also overlaid in MLAT/MLT coordinates. Magnetic north, south, west (dawn), and east (dusk) are marked in the Figure 1 (top row). Five throat auroras are observed in this time interval, but only three are shown in Figure 1 (see the dashed yellow lines in the red image) equatorward of the persistent E-W aligned auroral oval. In the green image, we notice some diffuse auroras (marked by arrows) with stripy features equatorward of the throat auroras, consistent with *Han et al*. [2015] who demonstrated that throat auroras are always observed in association with stripy diffuse auroras. A full evolution of the throat auroras is shown in Movies S1 (red line) and S2 (green line) of the supporting information.

3.1. Auroral Signatures in Response To the Solar Wind and IMF

Figures 2a–2c show the time-shifted solar wind density, speed, and IMF components. With an average solar wind speed of ~377 km/s, using an equation given by *Liou et al*. [1998] and adding ~10 min transit time of the solar wind from the bow shock to the magnetopause and from the magnetopause to the ionosphere, we must apply a ~75 ± 3 min solar wind propagation delay before signatures at ACE are seen in the ionosphere. This delay is also consistent with the auroral signatures at 08:55 UT in Figures 2d and 2e, i.e., that the sudden decrease of diffuse auroras and following increase of discrete auroras in Rayleigh intensities are corresponding to a polarity change in IMF B_z.

Keograms of the green and red auroras shown in Figures 2d and 2e are obtained by extracting all-sky image data along the geomagnetic meridian of Ny-Ålesund in an area that is one pixel wide. The blank area in Figure 2d is due to missing data. The horizontal dashed lines denote the zenith location of Ny-Ålesund. Indicated in Figures 2c and 2e, with horizontal magenta bars, are four intervals of red aurora emission enhancements, i.e., ~09:01:20–09:11:30 UT for interval *I*, ~09:17:20–09:20:10 UT for interval *II*, ~09:27:00–09:29:00 UT for interval *III*, and ~09:35:00–09:44:10 UT for interval *IV*. In intervals I and IV the equatorward motion of the red line is well correlated with the negative shift of IMF B_z, which is favorable for subsolar reconnection; while the enhancement of the red emissions in intervals II and III is more expected to be due to the rapid fluctuations of IMF B_y during the high-latitude magnetopause reconnection. With the equatorward motion of the discrete aurora such as in the interval I, the diffuse aurora with bright features can sometimes stretch poleward (see the arrows in Figure 2d). This has the resemblance of the stripy diffuse aurora described by *Han et al*. [2015]. However, the throat auroras in Figure 1 cannot be easily identified only from the keogram.

3.2. Throat Aurora Associated With Ionospheric Backscatter

In order to investigate the throat aurora in some detail, Figure 3 shows a sequence of two-dimensional images of the red line every 4 min, with spectral width data from the Finland HF radar overlaid. The magenta dots mark locations of enhanced spectral width (>150 m/s), and the black solid line represents
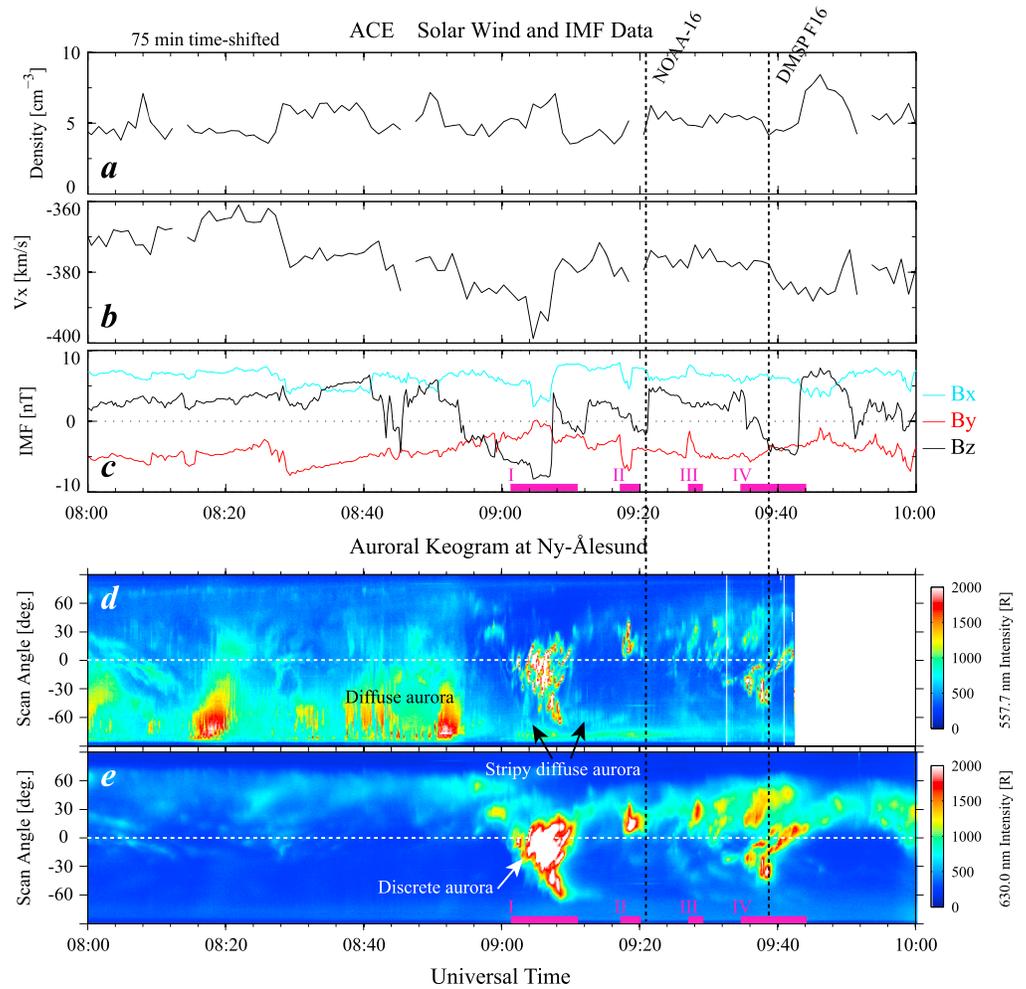
Figure 2. (a–c) Solar wind density, speed, and the interplanetary magnetic field (IMF) in geocentric solar magnetic (GSM) coordinates measured by ACE on 27 December 2003. The solar wind data have been time shifted using a 75 min time lag. (d and e) Keograms along the geomagnetic meridian of green and red line data from all-sky imagers.

the approximate location of MLN. It is generally believed that the boundary of the auroral oval is roughly a smooth curve [e.g., *Feldstein et al.*, 2014]. The general equatorward boundary of the auroral oval using weighted average is thus sketched as a black dotted curve in each image by identifying the maximum gradient of the auroral emission intensity along the geomagnetic meridian of Ny-Ålesund. The throat auroras can be easily identified equatorward of the auroral oval boundary.

The numbers and arrows denote the successively observed throat auroras. The first throat aurora (labeled "1") with a brightening feature started at 09:00:03 UT. A few minutes later (at 09:04:03 UT), the second and third throat auroras (labeled "2" and "3") are observed in the postnoon sector. For these three throat auroras, it is noticed that each throat aurora can span over ~2–3° in geomagnetic latitude (~71.5°–75.5° MLAT) assuming that the auroral height profile is reasonable. All throat auroras from high to low geomagnetic latitudes drift westward (i.e., toward MLN) with speeds on the order of tens to hundreds of meter per second. In addition, the ray-like first and third throat auroras move poleward and show brightening followed by dimming, which can be more clearly seen from Movie S1 in the supporting information. The first throat aurora at ~09:04 to 09:16 UT in Figure 3 is well colocated with enhanced spectral widths. The colocation between the third throat aurora and the enhanced spectral width is observed from ~09:04 to 09:12 UT, as well as at ~09:20 UT for their northern part. The rest of the time, the area of enhanced spectral widths, is sporadically observed equatorward of the auroral oval boundary.
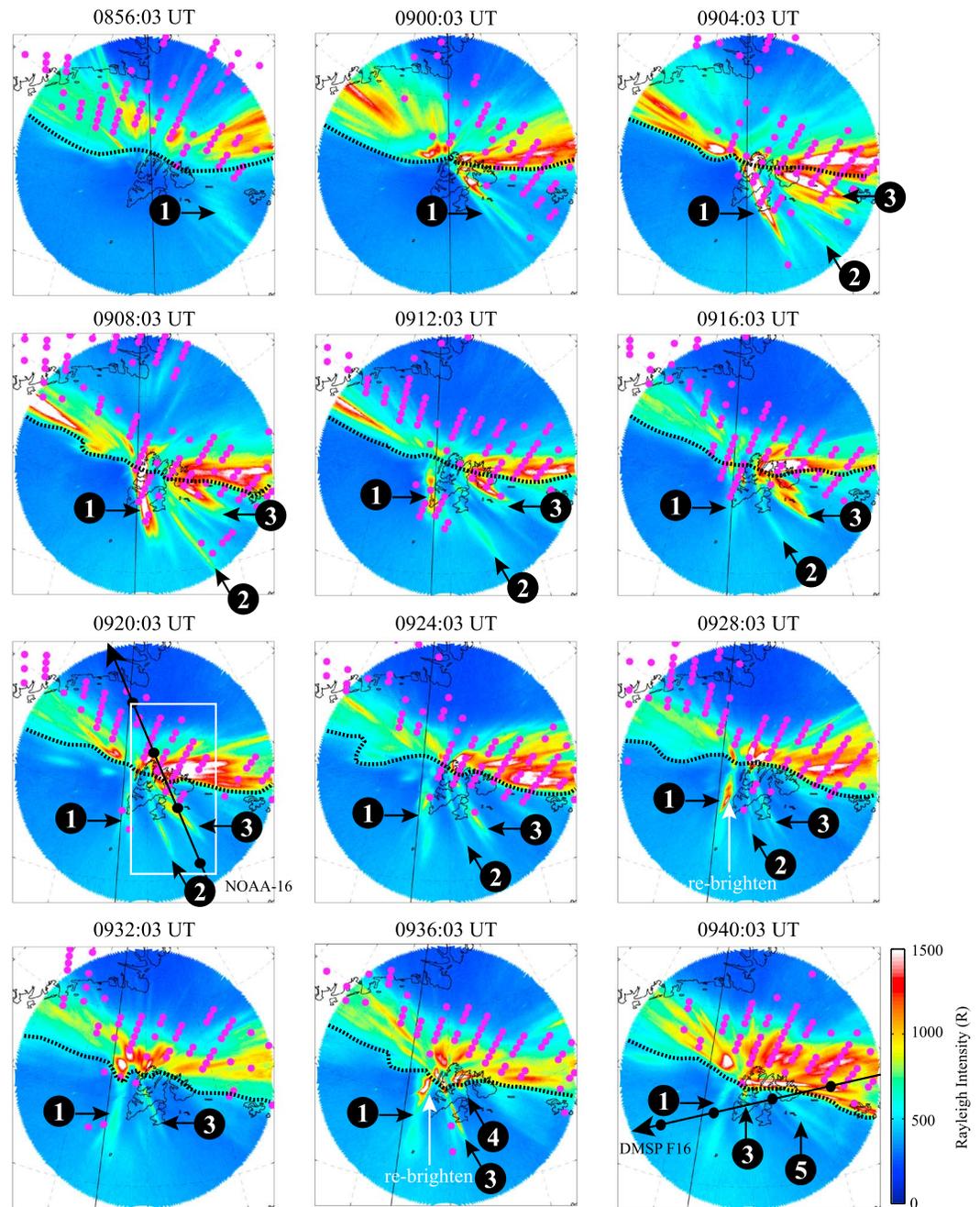
Figure 3. A sequence of red line throat aurora images every 4 min and using MLAT/MLT coordinates, with Finland radar spectral width data overlaid. The magenta dots mark locations of enhanced spectral width (>150 m/s). The black dotted curves illustrate the general auroral oval boundary, and the black solid line represents the approximate location of MLN. A sequence of throat auroras is labeled by numbers. The trajectories of NOAA 16 and DMSP F16 are also overlaid and mapped to the same height as the auroral emissions.

As mentioned in section 2 there are mapping uncertainties for both HF radar backscatter and the assumed auroral emission height, which means that we must be careful when we compare the colocation between the throat aurora and the enhanced spectral widths. Figure 4 shows simultaneous observation of the red line intensity and the ionospheric backscatter as a function of time (08:50–09:50 UT) and MLAT to verify their colocation. The intensity in Figure 4a is the same as Figure 2e, but it is mapped to MLAT based on the assumed 200 km emission height. Figures 4b and 4c show median-filtered ionospheric line-of-sight velocity and
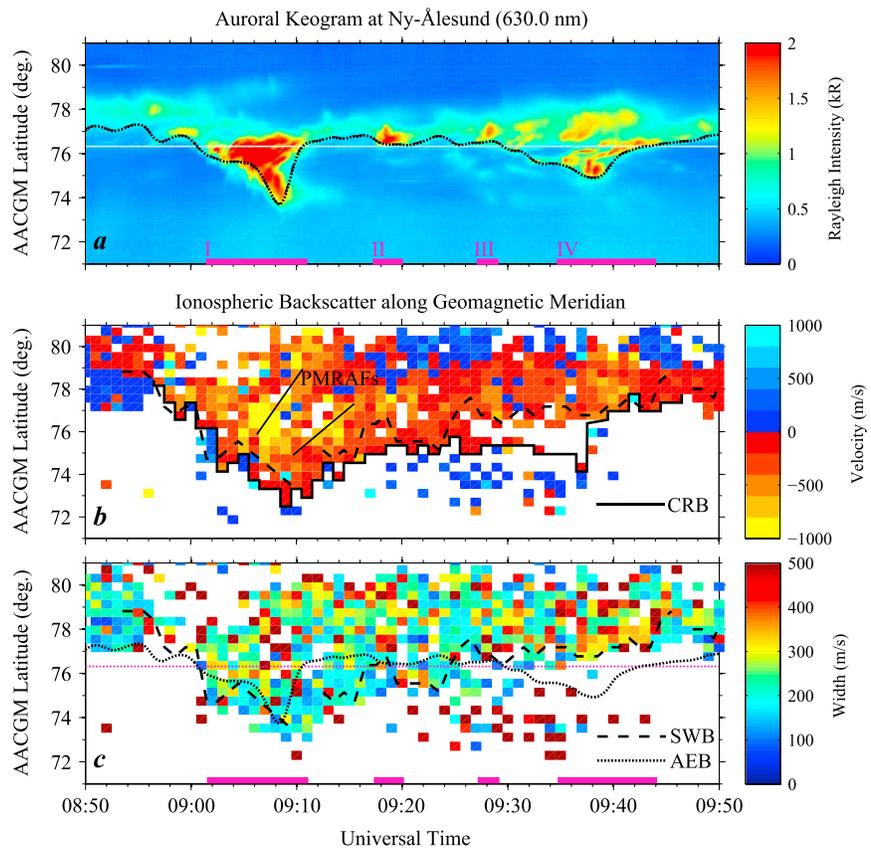
Figure 4. (a) The red line intensity along the geomagnetic meridian as a function of time and MLAT. The dotted curve represents the auroral equatorward boundary, which is also superimposed on Figure 4c. (b and c) Simultaneous measurements of the median-filtered line-of-sight velocity and spectral width along the geomagnetic meridian. Positive velocities are toward the radar. The dashed curve represents the spectral width boundary, while the short solid lines in Figure 4b show the structure of two poleward moving radar auroral forms. The convection reversal boundary is delineated by the solid line.

spectral width that are based on adjacent beam range gates close to the geomagnetic meridian (see *Chen et al.* [2015] for more details). Positive velocities are toward the radar. The black dotted curve in Figure 4a represents the auroral equatorward boundary (AEB), while the black dashed curve in Figures 4b and 4c represents the spectral width boundary (SWB). Although the AEB is still determined by the maximum in the gradient of the emission intensity, it is characteristic of the equatorward boundary of the red line emission along the geomagnetic meridian of Ny-Ålesund. This means that the AEB is sometimes different from the weighted-average auroral oval boundary shown in Figure 3, when the brightening throat aurora is not along the geomagnetic meridian. The SWB is determined by a certain spectral width threshold value (i.e., >150 m/s) [*Chisham and Freeman*, 2003], and a more reliable criterion has been considered by *Chen et al.* [2015]. The horizontal dashed lines in Figures 4a and 4c also denote the zenith location of Ny-Ålesund. In addition, the AEB in Figure 4a is also overlaid in Figure 4c for easy comparison of their colocation. The two-dimensional images in Figure 3 confirm that the enhanced red auroral emission in intervals I and IV represent the dynamic behaviors of the first and third throat auroras, respectively. During interval I both AEB and SWB shift equatorward to ~73.2° MLAT at ~09:09:20 UT. After that, with the northward turning of the IMF B_z, the brightening of the first throat aurora moves away from the geomagnetic meridian, and the AEB retreats to near zenith in Ny-Ålesund at ~09:10 UT. While the poleward motion of the SWB is slower than that of the AEB, the SWB moves to near zenith in Ny-Ålesund at ~09:16 UT. During the intervals II and III, both AEB and SWB are located in the vicinity of zenith in Ny-Ålesund. However, in the interval of ~09:20–09:24 UT, the SWB was located more equatorward at ~75.5° MLAT. The AEB in interval IV is characterized by the third throat aurora that shifts equatorward to
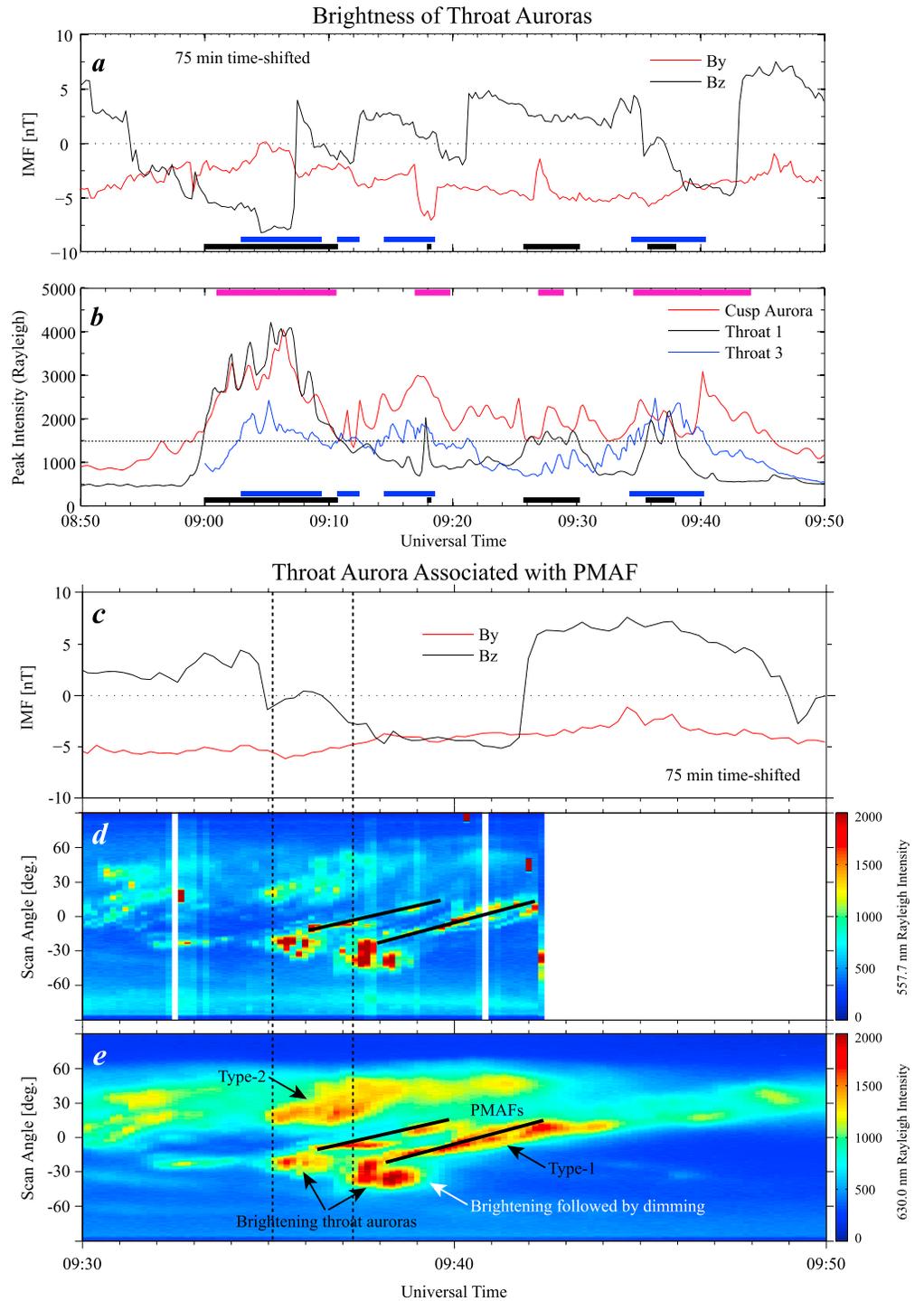
Figure 5. (a) The time-shifted IMF B_y and B_z components. (b) Time series of the peak emission intensities of the cusp aurora (red) and the first (black) and third (blue) throat auroras. The horizontal bars (black and blue) indicate times when the first and third throat auroras exceed 1500 Rayleigh in intensity. See text for a more detailed description. (c) The time-shifted IMF B_y and B_z components for the third throat aurora event. (d and e) Keograms along the magnetic meridian for the green and red emission lines, with the third throat aurora, PMAFs and type 1 and type 2 cusp auroras indicated.

~75° MLAT at ~09:38 UT. The SWB remains in the northward vicinity of Ny-Ålesund although there is also a small equatorward migration at ~09:38 UT.

3.3. The Relationship Between Throat Aurora and PMAFs

The first throat aurora with antisunward flow at ~09:02–09:09 UT is detected by ionospheric backscatter associated with poleward moving radar auroral forms [e.g., *Milan et al.*, 2000], which is denoted by the short black solid lines in Figure 4b. Sometimes, we also observe dim throat auroras that rebrighten, such as at 09:28:03 and 09:36:03 UT in Figure 3 (white arrows). The throat auroras have brightening and dimming features in auroral intensity, but without information on the vertical column emission profile of the throat aurora, we cannot make an accurate definition for the brightening and dimming properties of the throat auroras. To consider how the throat aurora brightening and dimming features are associated with signatures in the cusp aurora, Figure 5b shows time series of the peak emission intensities for different auroras, together with the time-shifted IMF B_y and B_z components (Figure 5a). Figures 5d and 5e give a zoom in of the green and red lines in the same format as Figures 2d and 2e for the time interval of 09:30–09:50 UT. Because auroral rays may affect the mapping of the aurora, here we use the peak emission intensities of the first and third throat auroras for comparison with the cusp aurora. The peak intensities for different auroral types can be identified because of separation of the first and third throat auroras, as well as the cusp aurora (see Figure 3). Thus, the throat aurora features can be compared with the cusp aurora.

In Figure 5b we see that the peak emission intensity of the cusp aurora (red line) can reach above 1500 Rayleigh during the interval of 09:00–09:40 UT. Thus, the throat auroras are considered as brightening when their peak emission intensity is above that value, as is marked by the thick horizontal bars. Colors black and blue correspond to the intervals of the first and third throat auroras, respectively. The intervals of the brightening throat auroras are almost aligned with enhancements of the red aurora in Figure 2 (i.e., the magenta horizontal bars in Figure 5b). On the other hand, the peak emission intensity of the dimming throat auroras is distinctly lower than 1500 Rayleigh and the intensity of the cusp aurora. Compared to the IMF conditions in Figure 5a, it is seen that most brightening throat auroras are associated with southward shifts of IMF B_z, although parts of the throat aurora may still be within the interval of northward IMF B_z.

The rebrightening of the third throat aurora starts at 09:36:03 UT and is aligned along the local geomagnetic meridian. This gives us a chance to survey the relations between the poleward moving throat aurora and the cusp PMAFs. At ~09:35–09:39 UT three different auroral emission regions are clearly shown in the red emission line (Figure 5e), which include the brightening of the third throat aurora 10°–45° south of zenith, the type 1 aurora with PMAFs in the close vicinity of zenith, and the type 2 aurora farther north (5°–50° north of zenith). In the literature the simultaneous presence of both type 1 and type 2 cusp aurora is referred to as a bifurcated or double cusp and it is believed to be due to the coexistence of subsolar and lobe reconnection driven by the B_y-dominated IMF orientation [*Sandholt et al.*, 2001; *Wing et al.*, 2001]. The throat aurora brightens twice and is roughly accompanied by two southward turnings of IMF B_z (indicated by the two vertical dashed black lines in Figure 5c). Both brightening are just prior to the formation of PMAFs (indicated by the tilted solid black lines in Figures 5d and 5e). The third throat aurora brightening is observed at ~09:39:00–09:39:30 UT in the red emission line and is followed by dimming that is consistent in time with particle precipitation detected by DMSP F16.

3.4. Throat Aurora in Relation To Particle Precipitation

The vertical dotted lines in Figure 2 indicate the times when NOAA 16 and DMSP F16 intersected the throat auroras, which give us a chance to investigate the particle precipitation. The orbits of both NOAA 16 and DMSP F16 have been traced down the field line to the assumed altitude of the red line emission, using AACGM.

3.4.1. NOAA 16

The NOAA 16 spacecraft intersected the third throat aurora and the cusp aurora as indicated in Figure 3. The trajectory of NOAA 16 is in the all-sky field of view at ~09:19:45–09:23:50 UT. Figures 6a–6d present the particle observations from NOAA 16. Figures 6a and 6c represent the fluxes of precipitating electrons and ions, respectively, in four energy channels (154–224, 688–1000, 2115–3075, and 6503–9457 eV). Figure 6b shows fluxes of magnetospheric electrons with energies >30 (black), >100 (red), and >300 (green) keV, and Figure 6d shows the flux of magnetospheric ions with energies between 30 and 80 keV. In Figures 6b and 6d,
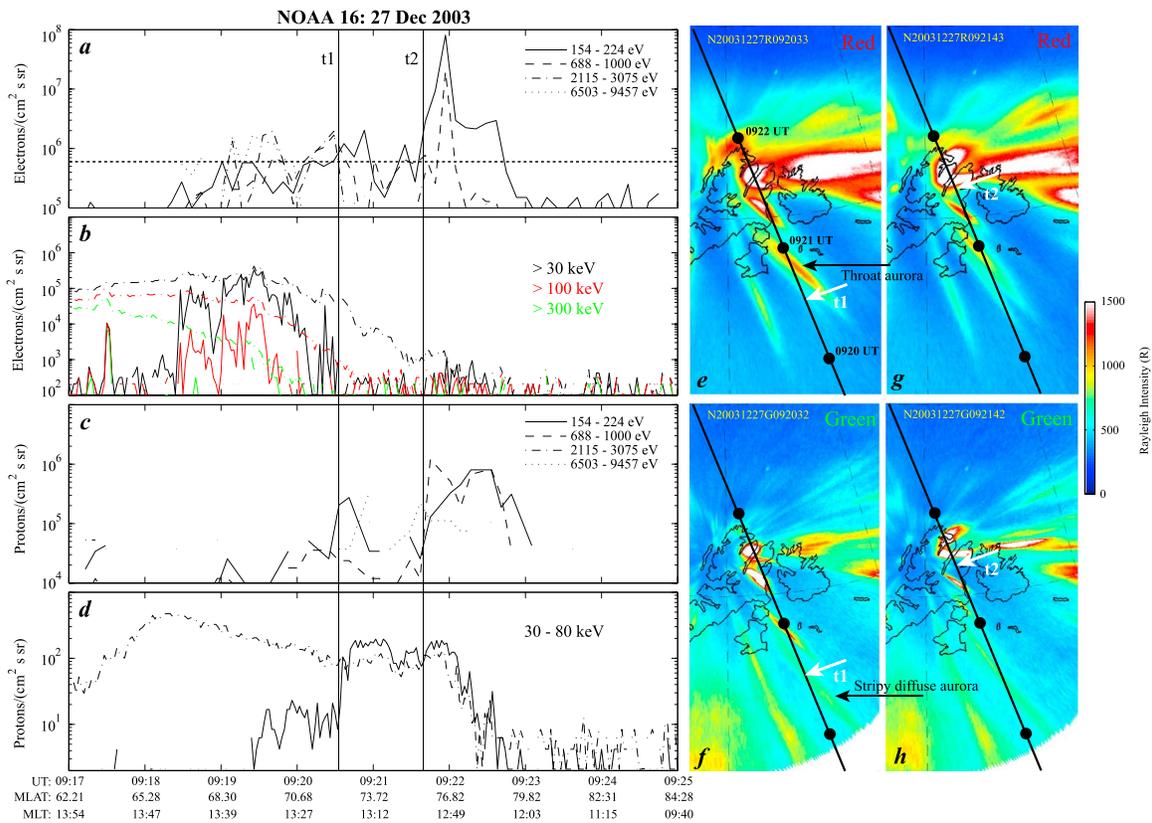
Figure 6. (a–d) Electron and proton observations from NOAA 16. (e–h) Zoom-in panels of the all-sky data (equal to the white rectangle in Figure 3) at 09:20:33 and 09:21:43 UT for the (e and g) red and (f and h) green emission lines. The white arrows match the equatorward edges of the third throat aurora and the cusp auroral oval, also shown by the two vertical lines t1 and t2 in Figures 6a–6d.

the solid and dashed curves represent fluxes measured at pitch angles near 10° and 80°, respectively. The vertical solid lines at "t1" (09:20:32 UT) and "t2" (09:21:40 UT) indicate when the satellite entered the third throat aurora and the cusp aurora, respectively. t1 and t2 are also marked by white arrows in Figures 6e–6f (09:20:33 UT) and 6g–6h (09:21:43 UT), which are zoom-in panels of the all-sky data corresponding to the white rectangle at 09:20:03 UT in Figure 3.
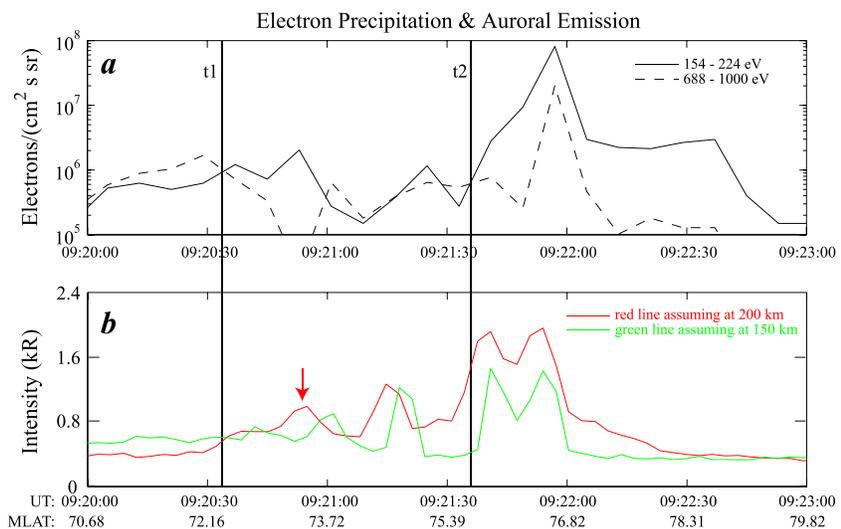
Figure 7. (a) Electron precipitation fluxes at 154–224 and 688–1000 eV from NOAA 16. (b) The red and green line auroral intensities along the trajectory of NOAA 16. See text for more details.
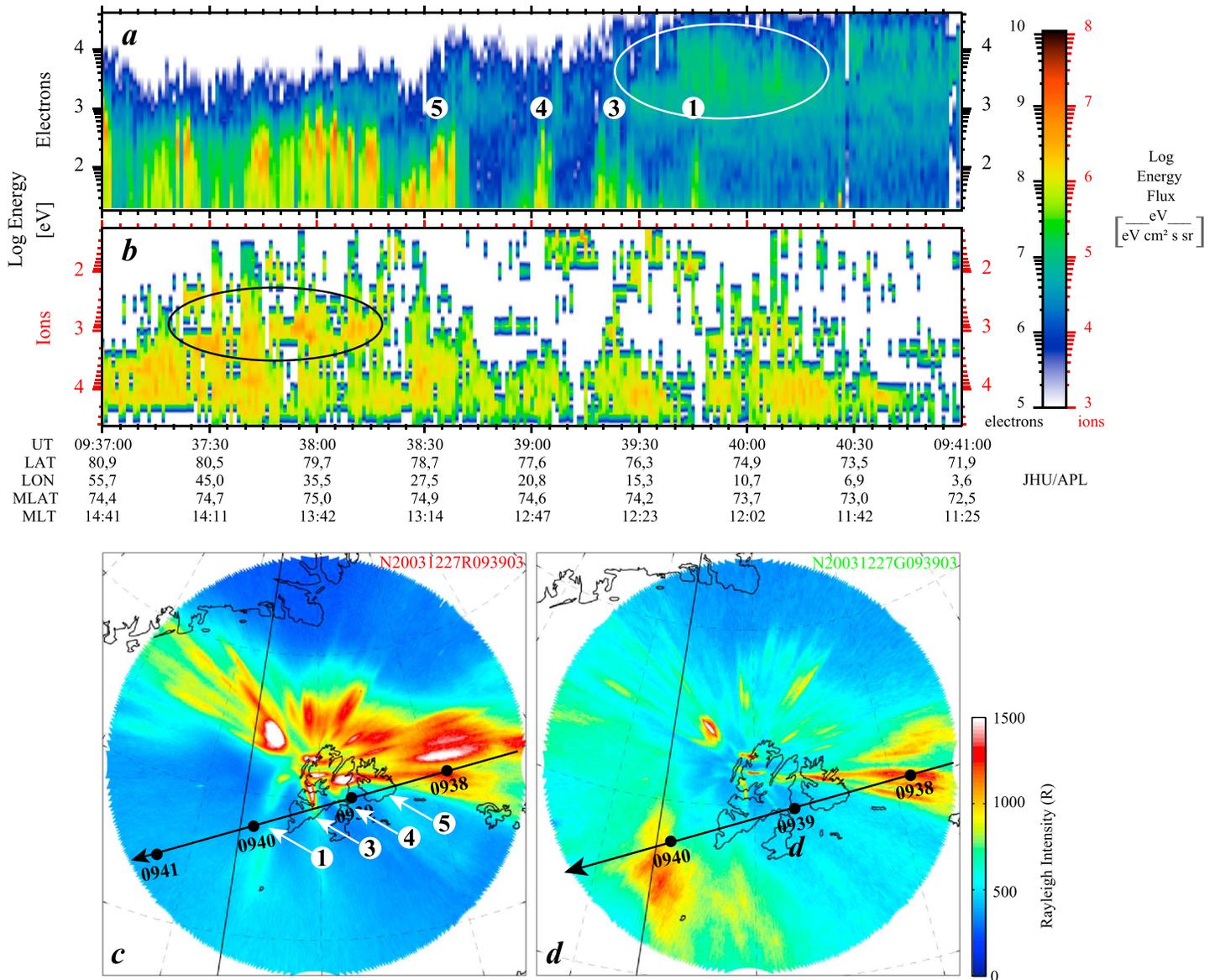
Figure 8. (a and b) Fluxes of precipitating electrons and ions at energies between 30 eV and 30 keV recorded by DMSP F16. (c and d) All-sky images of the red and green emission lines captured at 09:39 UT, with the DMSP F16 track overlaid. The four white arrows mark the corresponding throat auroras (1, 3, 4, and 5).

To compare the brightness of the throat aurora and the cusp aurora with the electron precipitation, Figure 7 presents time series of the flux of magnetosheath-like electrons at 154–224 and 688–1000 eV (Figure 7a), together with the red and green line auroral intensity along the trajectory of the NOAA 16 spacecraft (Figure 7b). The auroral brightness along the satellite track is extracted from mapped auroral images by using the pixel intensity closest to the point of the field line traced satellite. Due to the spatial and temporal evolutions of the auroral brightness, we have used mapped images every 10 s.

At t1 the throat aurora boundary corresponds to a transition from particles at energies >688 eV to energies <224 eV. It is also aligned with the poleward boundary of precipitating >30 keV magnetospheric electrons (the solid black curve in Figure 6b). As electrons with energies between 0.5 and a few keV are the source of the 557.7 nm emissions, the stripy diffuse aurora (denoted in Figure 6f) farther equatorward of t1 is collocated with precipitation of magnetospheric electrons, which is in favor of closed field lines. The third throat aurora around 09:20:53 UT (i.e., the red arrow in Figure 7b) is associated with precipitation of 154–224 eV low-energy electrons mixed with minor fluxes of near-isotropic magnetospheric ions (>30 keV in Figure 6d),

which is a typical signature of the low-latitude boundary layer (LLBL). Measurements at t2 show typical cusp dispersion signatures, which are characterized by bands of magnetosheath ion precipitation showing decreased energy with increased latitude (t2—09:23 UT; see Figure 6c).

3.4.2. DMSP F16

The DMSP F16 spacecraft traversed a sequence of dimming throat auroras from postnoon to MLN at ~09:37:20–09:41:10 UT (see Figure 3). Figures 8a and 8b show the electron and ion precipitation data from DMSP F16. Figures 8c and 8d show mapped images of the red and green line auroras at 09:39:03 UT. DMSP F16 observed precipitation of moderate beam-like magnetosheath electrons and magnetosheath ions (see the black ellipse in Figure 8b) before it traversed the dimming throat auroras. It is consistent with the discrete aurora in the right side of Figure 8c (i.e., to the east) being on open field lines. Four throat auroras with dimming features (labeled "5," "4," "3," and "1") are centered at 09:38:30, 09:39:02, 09:39:22, and 09:39:45 UT. Events 1 and 3 were also reported in Figure 3, while event 2 vanished at ~09:30 UT. All four dimming throat auroras are associated with high fluxes of magnetosheath-like 30–500 eV electrons and no precipitation of magnetosheath ions. For the dimming throat aurora labeled 5 the flux of magnetosheath electrons is significantly higher than for the other events, but it is also located at higher latitudes and closer to the cusp aurora.

4. Discussion

In this paper, we report a sequence of throat aurora observed near MLN (i.e., 1200–1240 MLT) on 27 December 2003. The throat auroras are always located equatorward of the general discrete dayside auroral oval. By examining the dynamic properties of the throat aurora in the red line, we find that the throat auroras with a poleward moving form normally consist of a brightening followed by dimming feature (see Figure 3 and Movie S1 in the supporting information). Observations show that, sometimes, the brightening of the throat auroras is well colocated with enhanced spectral width as seen by SuperDARN Finland radar (interval I), and it is a precursor of PMAFs (interval IV). By comparing the brightness of the throat auroras with the varying IMF conditions, both the throat aurora brightening and dimming processes are occurring not only for southward IMF B_z but also for northward IMF (see Figures 5a and 5b). While the brightening throat aurora associated with PMAFs (intervals I and IV in Figure 5) is more attributed to the negative shift of IMF B_z, this dynamic nature implies that the brightening throat aurora is likely related to low-latitude magnetopause reconnection. Ionospheric signatures of transient magnetopause reconnection are often associated with pulses in dayside reconnection rate and plasma flow such as PMAFs and poleward moving radar auroral forms [*Lockwood et al.*, 1995; *Milan et al.*, 2000; *Moen et al.*, 1995, 2008; *Oksavik et al.*, 2004a; *Pinnock et al.*, 1995; *Rinne et al.*, 2007]. The transient brightening of the throat auroras is associated with PMAFs (interval I in Figure 4b) and equatorward of it (interval IV in Figure 5d), while the throat aurora-related AEB is colocated with the SWB in interval I in Figure 4c. These lead us to consider whether the brightening and dimming of the throat auroras are on open and closed field lines, respectively.

4.1. The Brightening Throat Auroras and Its Associated Ionospheric Spectral Width

Previous studies have confirmed that the equatorward boundaries of cusp auroral emissions and the transition from narrow to broad spectral width are good empirical proxies for the ionospheric open/closed field line boundary (OCB) [e.g., *Baker et al.*, 1995; *Lorentzen et al.*, 1996; *Yeoman et al.*, 1997]. It is well known that the cusp auroral signatures are an important indicator of magnetopause reconnection on open field lines [e.g., *Newell and Meng*, 1995; *Sandholt and Newell*, 1992]. The intimate colocation between the equatorward edge of the HF radar cusp and the cusp aurora has also been confirmed by many studies [e.g., *Milan et al.*, 1999; *Moen et al.*, 2001, 2002; *Oksavik et al.*, 2004b; *Rodger et al.*, 1995; *Yeoman et al.*, 1997]. In Figure 4, simultaneous 630.0 nm AEB and HF radar SWB measurements show that the AEB in the vicinity of zenith is well colocated with the SWB (intervals II and III), which means that the cusp aurora is very likely on open field lines. The first throat aurora brightening is well colocated with large spectral widths (interval I), but this colocation is not well established in interval IV for the brightening of the third throat aurora, which is most likely attributed to the mapping accuracy of the HF radar echoes.

After 09:30 UT, the SWB is always poleward of the AEB, which can be due to the fact that the mapping of HF radar echoes does not take into account the prevailing conditions for radio wave propagation in the cusp ionosphere, and transient magnetopause reconnection can increase the inflow of high-density plasma

which causes enhanced refraction of HF radio signal and worse mapping accuracy [*Chen et al.*, 2015]. Moreover, plasma patches with higher density than the background are known to exist in the dark cusp near MLN [*Carlson et al.*, 2002; *Lockwood et al.*, 2005a, 2005b; *Lorentzen et al.*, 2010; *Moen et al.*, 2006; *Oksavik et al.*, 2006, 2010, 2015; *Zhang et al.*, 2011, 2013] and create space weather challenges in the polar ionosphere [*Moen et al.*, 2013]. Both the AEB and the SWB observed an equatorward migration at ~09:38 UT, which means that the SWB may delineate the motion of the OCB at this time, but the SWB is overestimated. The PMAFs in Figure 5e must be on open field lines due to magnetopause reconnection; however, the PMAFs are suggested to be on closed field lines if only identified by the SWB.

The colocation of AEB and SWB is well observed in interval I. Although we have assumed that the 630.0 nm emissions are concentrated around an altitude of 200 km for the throat aurora, the altitude of the red line emission in the cusp may range from 200 to 400 km or even higher [e.g., *Carlson et al.*, 2013]. The upper part of a tall auroral ray bundle will appear at a shorter radial distance from the observing site, and the bottom part will be mapped farther away. For throat auroras we have therefore chosen the bottom part of the red line emission where the mapping will be most accurate. To estimate the mapping error, we use intensity profiles modeled by *Johnsen et al.* [2012], which show that the red line emission is most peaking at ~256 km altitude southward of the observing site. Thus, the mapping uncertainty for the assumed emission height is about 28% (i.e., the mapping error is $\Delta_{mlat\_200} \times (256 - 200)/200$, where Δ_{mlat_200} represents the latitudinal span of the throat aurora). For the southernmost point of the AEB at 73.2° MLAT (interval I in Figure 4), it means that the mapped auroral uncertainties should be equatorward to within 0° to ~0.84°. If so, the mapping of the SWB will be overestimated by ~0.84° at most. If we move the AEB equatorward by ~0.84° (i.e., two range gates), the AEB will still be well colocated with the ionospheric backscatter. It means that the brightening throat aurora is well colocated with the ionospheric backscatter, at least in time interval I.

4.2. The Throat Aurora and Its Associated Dynamic Properties

Since the magnetopause maps to the ionosphere through the cusp, phenomena occurring at the equatorward boundaries of the cusp provide two-dimensional images of merging activity. In intervals I in Figure 4 and IV in Figure 5 the time evolution of the throat aurora indicates an intimate relationship from the initial brightening of the throat aurora to the subsequent development of PMAFs. This process is very similar to the fine structure of auroral transients at the cusp equatorward boundary reported by *Moen et al.* [1996] and *Sandholt et al.* [2002]. Low-latitude magnetopause reconnection is expected under the negative IMF B_z conditions [*Lockwood*, 1998; *Newell and Meng*, 1998; *Onsager and Lockwood*, 1997], and both *Moen et al.* [1996] and *Sandholt et al.* [2002] reported that auroral transient events were characterized by recurrent (2–3 min) equatorward boundary intensifications, and they suggested that the auroral transients are related to LLBL on open field lines. Particle data from NOAA 16 in Figure 6 also indicate that the throat aurora was in the LLBL. *Sandholt et al.* [2002] observed an ~100 km wide gap in latitude between the auroral fine structure and the diffuse aurora, which was suggested to be due to a loss of plasma sheet particles along newly open field lines that is faster than the entry of magnetosheath particles along open field lines [*Gosling et al.*, 1990], as the open field lines move poleward. This scenario is not seen in our study. To the contrary, the throat aurora brightening is followed by dimming and the associated stripy diffuse aurora at the equatorward side of it (see Figure 6 images). *Han et al.* [2016] suggested that the throat aurora should occur when cold magnetospheric plasma is flowing into the magnetopause reconnection site. From the current optical and particle observations, the equatorward part of the brightening throat aurora followed by dimming manifests the residual of magnetosheath-like particles in this region, which may indicate some effects of cold magnetospheric plasma interaction with magnetic reconnection.

Previous studies [*Milan et al.*, 1999; *Thorolfsson et al.*, 2000] have already associated a poleward moving auroral transient with a narrow flow channel in SuperDARN data but without specifying their location relative to each other. Here we present a detailed observation on the relative location of the ionospheric signatures between the red line and HF radar backscatter. At ~72°–76° MLAT in Figure 4b and 09:00–09:40 UT, we observed that the brightening throat aurora is located well inside the poleward flow before 09:18 UT, while the dimming throat aurora is located in the vicinity or southward of the convection reversal boundary (CRB) after that (see the convection map in Figure 1). The CRB is a feature of the ionospheric convection pattern that separates sunward (i.e., equatorward) plasma flow from antisunward (i.e., poleward) plasma flow (see

the solid line in Figure 4b), which originates from distinct magnetospheric regions [e.g., *Newell et al.*, 1991]. The existence of equatorward return flow is suggested to be outside a newly opened reconnected flux tube as modeled by *Southwood* [1987], while the newly opened flux tube is convecting poleward under the influence of the reconnection electric field [e.g., *Rodger and Pinnock*, 1997]. If the enhanced electron precipitation of the brightening throat aurora is controlled by the pulsed reconnection electric field, the motion of the brightening throat aurora should follow the $E \times B$ convection drift. To simplify our consideration, in Figure 4b, using the SuperDARN line-of-sight velocity during the interval 09:00–09:12 UT we find a velocity of ~273 m/s on average in the poleward direction of the CRB. SuperDARN HF radars can underestimate the velocity by ~20%, because the refractive index in the scattering volume has not been taken into account [*Gillies et al.*, 2011]. During this time interval the convection electric field will shift the ionospheric plasma poleward by at least 2.34° in latitude. This is consistent with the latitudinal extent of the first brightening throat aurora.

4.3. The Dimming Throat Auroras and Its Associated Particle Precipitation

For the dimming throat auroras we look at the particle measurements from NOAA 16 and DMSP F16. The NOAA 16 particle data in Figure 6 show that the dimming of the third throat aurora at 09:20:53 UT is associated with weak precipitation of magnetosheath-like electrons (see also Figure 7b) mixed with intense precipitation of magnetospheric ions (>30 keV). The DMSP F16 particle data in Figure 8 show that the dimming of the third throat auroras is associated with decreased fluxes of magnetosheath-like electrons, accompanied with fluxes of magnetospheric electrons, which is sometimes referred to as the trapping boundary [*Nishida et al.*, 1993]. The trapping boundary is never located poleward of the LLBL [*Lockwood et al.*, 1996; *Onsager and Lockwood*, 1997]. Nevertheless, there is no detection of any magnetosheath ion precipitation in the NOAA 16 and DMSP F16 data.

An important characteristic of magnetosheath particles on newly open field lines is the ion energy dispersion [*Lockwood et al.*, 1998; *Newell and Meng*, 1991, 1995]. In Figure 6c this signature was only observed at t2, which also suggests that the dimming throat aurora could be on closed field lines. By using simultaneous low-altitude satellite and ground-based all-sky images, *Han et al.* [2016] have confirmed that the throat aurora is associated with low-energy electron and ion precipitation of magnetosheath origin on open field lines. However, they only provided a "snapshot" of the throat aurora, and they did not compare the intensity of the throat auroras to the cusp aurora. In our study the time series in Figure 7 show that the dimming throat aurora is much weaker in intensity than the cusp aurora, which is caused by soft electron precipitation. When comparing the data sets in Figure 7, we should pay attention to the potential mapping error arising from our assumption of a fixed auroral emission height, instead of a vertical column emission profile. Moreover, there is also a slight difference and offset in time resolution between the two data sets: 8–16 s time resolution for the NOAA 16 data and 10 s time resolution for the optical data (so some misalignment is expected). The high fluxes of magnetosheath-like electrons at 09:21:25 UT in Figure 7a appear to be slightly offset compared to the auroral emission at ~09:21:14–09:21:22 UT in Figure 7b. However, the chosen mapping altitude appears to be quite reasonable for the throat aurora and the cusp aurora.

We noticed that a dimming of the third throat aurora shown in Figure 8 is accompanied by a rapid poleward contraction of the brightening throat auroras (see also Movie S1). The dimming throat aurora was associated with precipitation of magnetosheath-like electrons with energies of 30–500 eV detected by DMSP F16 (and 154–224 eV detected by NOAA 16) and could be due to pitch angle scattering on closed magnetic field lines. The cross-field diffusion of magnetosheath-like plasma can be supported by wave particle interaction between low-frequency waves and a steady state plasma source of the LLBL [*Tsurutani et al.*, 1989]. The particle data in Figure 6a also illustrate that the magnetosheath-like electrons associated with the generation of throat aurora can penetrate to much lower latitude [*Han et al.*, 2016; *Lyons et al.*, 1994]. It shows that the flux of 154–224 eV magnetosheath-like electrons has some weak fluctuations before t1 (see the spikes intersecting the horizontal dotted line). Magnetosheath-like electrons in the magnetosphere are possibly caused by high-latitude magnetopause reconnection before 08:54 UT due to prolonged periods of northward IMF B_z [*Shi et al.*, 2009, 2013; *Øieroset et al.*, 2008]. *Øieroset et al.* [2008] suggested that when the IMF clock angle is as large as 60 (i.e., northward with a strong IMF B_y component) the solar wind particles can enter across the dayside magnetopause through a reconnection site either poleward of both cusps or poleward of one cusp in one hemisphere and equatorward of the cusp in

the other. Magnetosheath-like electrons inside the CPS were also detected by NOAA 16 when it traversed the east coast of Svalbard at ~07:40 UT (data not shown), which is similar to the event we presented at ~09:20 UT in Figure 5. The ground-based data also confirm that the fairly dim auroral emissions appear at the equatorward side (70°–75° MLAT) of the auroral oval in the postnoon sector before 09:00 UT (see first image in Figure 3).

5. Conclusion

In this paper we report a sequence of throat auroras near MLN (1200–1240 MLT) on 27 December 2003. By examining the dynamic properties of throat aurora, and comparing with earlier studies [Han et al., 2016], we find that the dynamic process of throat auroras consists of brightening and dimming features. Simultaneous HF radar measurements show that the brightening throat aurora is colocated with the region of enhanced spectral widths, while its poleward motion follows the ionospheric $E \times B$ convection drift. The throat aurora is sometimes a precursor of PMAF. Particle observations from NOAA 16 show that the dimming throat aurora is associated with precipitation of injected magnetosheath-like electrons mixed with magnetospheric ions (see Figure 6). The dimming of the throat aurora is followed by a poleward contraction of the brightening throat aurora, with more precipitation of magnetosheath electrons than magnetospheric electrons detected by DMSP F16. Based on the observations of the ionospheric $E \times B$ poleward drift and comparison of the AEB and the SWB in intervals I and IV, we suggest that the brightening throat auroras are likely on open field lines. However, the NOAA and DMSP observations as well as CRB locations suggest that dimming auroras are related to the LLBL on closed field lines.

References

Baker, K. B., J. R. Dudeney, R. A. Greenwald, M. Pinnock, P. T. Newell, A. S. Rodger, N. Mattin, and C. I. Meng (1995), HF radar signatures of the cusp and low-latitude boundary layer, J. Geophys. Res., 100(A5), 7671–7695, doi:10.1029/94JA01481.

Borovsky, J. E., and M. H. Denton (2006), Effect of plasmaspheric drainage plumes on solar-wind/magnetosphere coupling, Geophys. Res. Lett., 33, L20101, doi:10.1029/2006GL026519.

Carlson, H. C., K. Oksavik, J. Moen, A. P. van Eyken, and P. Guio (2002), ESR mapping of polar-cap patches in the dark cusp, Geophys. Res. Lett., 29(10), 1386, doi:10.1029/2001GL014087.

Carlson, H. C., K. Oksavik, and J. I. Moen (2013), Thermally excited 630.0 nm O(1D) emission in the cusp: A frequent high-altitude transient signature, J. Geophys. Res. Space Physics, 118, 5842–5852, doi:10.1002/jgra.50516.

Chen, X. C., D. A. Lorentzen, J. I. Moen, K. Oksavik, and L. J. Baddeley (2015), Simultaneous ground-based optical and HF radar observations of the ionospheric footprint of the open/closed field line boundary along the geomagnetic meridian, J. Geophys. Res. Space Physics, 120, 9859–9874, doi:10.1002/2015JA021481.

Chen, X. C., D. A. Lorentzen, J. I. Moen, K. Oksavik, L. J. Baddeley, and M. Lester (2016), F region ionosphere effects on the mapping accuracy of SuperDARN HF radar echoes, Radio Sci., 51, 490–506, doi:10.1002/2016RS005957.

Chisham, G., and M. P. Freeman (2003), A technique for accurately determining the cusp-region polar cap boundary using SuperDARN HF radar measurements, Ann. Geophys., 21(4), 983–996, doi:10.5194/angeo-21-983-2003.

Chisham, G., T. K. Yeoman, and G. J. Sofko (2008), Mapping ionospheric backscatter measured by the SuperDARN HF radars—Part 1: A new empirical virtual height model, Ann. Geophys., 26(4), 823–841, doi:10.5194/angeo-26-823-2008.

Demekhov, A., and V. Y. Trakhtengerts (1994), A mechanism of formation of pulsating aurorae, J. Geophys. Res., 99(A4), 5831–5841, doi:10.1029/93JA01804.

Evans, D. S., and M. S. Greer (2000), Polar Orbiting Environmental Satellite Space Environment Monitor-2: Instrument Description and Archive Data Documentation, Tech. Memo. OAR SEC-93, NOAA, Boulder, Colo.

Feldstein, Y., V. Vorobjev, V. Zverev, and M. Förster (2014), Investigations of the auroral luminosity distribution and the dynamics of discrete auroral forms in a historical retrospective, Hist. Geo Space Sci., 5(1), 81, doi:10.5194/hgss-5-81-2014.

Fuselier, S., J. Burch, P. Cassak, J. Goldstein, R. Gomez, K. Goodrich, W. Lewis, D. Malaspina, J. Mukherjee, and R. Nakamura (2016), Magnetospheric ion influence on magnetic reconnection at the duskside magnetopause, Geophys. Res. Lett., 43, 1435–1442, doi:10.1002/2015GL067358.

Gillies, R. G., G. C. Hussey, G. J. Sofko, P. V. Ponomarenko, and K. A. McWilliams (2011), Improvement of HF coherent radar line-of-sight velocities by estimating the refractive index in the scattering volume using radar frequency shifting, J. Geophys. Res., 116, A01302, doi:10.1029/2010JA016043.

Gosling, J., M. Thomsen, S. Bame, T. Onsager, and C. Russell (1990), The electron edge of the low latitude boundary layer during accelerated flow events, Geophys. Res. Lett, 17(11), 1833–1836, doi:10.1029/GL017i011p01833.

Greenwald, R. A., et al. (1995), DARN/SuperDARN: A global view of the dynamics of high-latitude convection, Space Sci. Rev., 71(1–4), 761–796, doi:10.1007/BF00751350.

Han, D. S., X. Chen, J. Liu, Q. Qiu, K. Keika, Z. Hu, J. Liu, H. Hu, and H. Yang (2015), An extensive survey of dayside diffuse aurora based on optical observations at Yellow River Station, J. Geophys. Res. Space Physics, 120, 7447–7465, doi:10.1002/2015JA021699.

Han, D. S., Y. Nishimura, L. R. Lyons, H. Q. Hu, and H. G. Yang (2016), Throat aurora: The ionospheric signature of magnetosheath particles penetrating into the magnetosphere, Geophys. Res. Lett., 43, 1819–1827, doi:10.1002/2016GL068181.

Han, D. S., H. Hietala, X. C. Chen, Y. Nishimura, L. R. Lyons, J. J. Liu, H. Q. Hu, and H. G. Yang (2017), Observational properties of dayside throat aurora and implications on the possible generation mechanisms, J. Geophys. Res. Space Physics, 122, doi:10.1002/2016JA023394.

Hardy, D. A. (1984), Precipitating electron and ion detectors (SSJ/4) for the block 5D/flights 6-10 DMSP satellites: Calibration and data presentation, *Rep. AFGL-TR-84-0317*, Air Force Geophys. Lab., Hanscom Air Force Base, Mass.

Horne, R., R. Thorne, N. Meredith, and R. Anderson (2003), Diffuse auroral electron scattering by electron cyclotron harmonic and whistler mode waves during an isolated substorm, *J. Geophys. Res.*, *108*(A7), 1290, doi:10.1029/2002JA009736.

Hu, Z. J., et al. (2009), Synoptic distribution of dayside aurora: Multiple-wavelength all-sky observation at Yellow River Station in Ny-Ålesund, Svalbard, *J. Atmos. Sol. Terr. Phys.*, *71*(8–9), 794–804, doi:10.1016/j.jastp.2009.02.010.

Johnsen, M. G., D. A. Lorentzen, J. M. Holmes, and U. P. Løvhaug (2012), A model based method for obtaining the open/closed field line boundary from the cusp auroral 6300 Å[OI] red line, *J. Geophys. Res.*, *117*, A03319, doi:10.1029/2011JA016980.

Li, B., et al. (2013), Inverted-V and low-energy broadband electron acceleration features of multiple auroras within a large-scale surge, *J. Geophys. Res. Space Physics*, *118*, 5543–5552, doi:10.1002/jgra.50517.

Li, W., et al. (2010), THEMIS analysis of observed equatorial electron distributions responsible for the chorus excitation, *J. Geophys. Res.*, *115*, A00F11, doi:10.1029/2009JA014845.

Liang, J., V. Uritsky, E. Donovan, B. Ni, E. Spanswick, T. Trondsen, J. Bonnell, A. Roux, U. Auster, and D. Larson (2010), THEMIS observations of electron cyclotron harmonic emissions, ULF waves, and pulsating auroras, *J. Geophys. Res.*, *115*, A10235, doi:10.1029/2009JA015148.

Liang, J., E. Donovan, Y. Nishimura, B. Yang, E. Spanswick, K. Asamura, T. Sakanoi, D. Evans, and R. Redmon (2015), Low-energy ion precipitation structures associated with pulsating auroral patches, *J. Geophys. Res. Space Physics*, *120*, 5408–5431, doi:10.1002/2015JA021094.

Liou, K., P. T. Newell, C. I. Meng, M. Brittnacher, and G. Parks (1998), Characteristics of the solar wind controlled auroral emissions, *J. Geophys. Res.*, *103*(A8), 17,543–17,557, doi:10.1029/98JA01388.

Lockwood, M. (1998), Identifying the open-closed field line boundary, in *Polar Cap Boundary Phenomena*, edited by J. Moen et al., 73 pp., Kluwer Acad., Norwell, Mass.

Lockwood, M., S. Cowley, M. Smith, R. Rijnbeek, and R. Elphic (1995), The contribution of flux transfer events to convection, *Geophys. Res. Lett.*, *22*(10), 1185–1188, doi:10.1029/95GL01008.

Lockwood, M., S. Cowley, and T. Onsager (1996), Ion acceleration at both the interior and exterior Alfvén waves associated with the magnetopause reconnection site: Signatures in cusp precipitation, *J. Geophys. Res.*, *101*(A10), 21,501–21,513, doi:10.1029/96JA01948.

Lockwood, M., S. Fuselier, A. Walker, and F. Søraas (1998), A summary of the NATO ASI on polar cap boundary phenomena, in *Polar Cap Boundary Phenomena*, edited by J. Moen et al., 415 pp., Kluwer Acad., Norwell, Mass.

Lockwood, M., J. Davies, J. Moen, A. Van Eyken, K. Oksavik, I. McCrea, and M. Lester (2005a), Motion of the dayside polar cap boundary during substorm cycles: II. Generation of poleward-moving events and polar cap patches by pulses in the magnetopause reconnection rate, *Ann. Geophys.*, *23*(11), 3513–3532, doi:10.5194/angeo-23-3513-2005.

Lockwood, M., J. Moen, A. Van Eyken, J. Davies, K. Oksavik, and I. McCrea (2005b), Motion of the dayside polar cap boundary during substorm cycles: I. Observations of pulses in the magnetopause reconnection rate, *Ann. Geophys.*, *23*(11), 3495–3511, doi:10.5194/angeo-23-3495-2005.

Lorentzen, D. A., and J. Moen (2000), Auroral proton and electron signatures in the dayside aurora, *J. Geophys. Res.*, *105*(A6), 12,733–12,745, doi:10.1029/1999JA900405.

Lorentzen, D. A., C. S. Deehr, J. I. Minow, R. W. Smith, H. C. Stenbaek-Neielsen, F. Sigernes, R. L. Arnoldy, and K. Lynch (1996), SCIFER-dayside auroral signatures of magnetospheric energetic electrons, *Geophys. Res. Lett.*, *23*(14), 1885–1888, doi:10.1029/96GL00593.

Lorentzen, D. A., J. Moen, K. Oksavik, F. Sigernes, Y. Saito, and M. G. Johnsen (2010), In situ measurement of a newly created polar cap patch, *J. Geophys. Res.*, *115*, A12323, doi:10.1029/2010JA015710.

Lui, A., P. Perreault, S.-I. Akasofu, and C. Anger (1973), The diffuse aurora, *Planet. Space Sci.*, *21*(5), 857–861, doi:10.1016/0032-0633(73)90102-5.

Lyons, L., M. Schulz, D. Pridmore-Brown, and J. Roeder (1994), Low-latitude boundary layer near noon: An open field line model, *J. Geophys. Res.*, *99*(A9), 17,367–17,377, doi:10.1029/94JA00867.

McComas, D., S. Bame, P. Barker, W. Feldman, J. Phillips, P. Riley, and J. Griffee (1998), Solar wind electron proton alpha monitor (SWEPAM) for the Advanced Composition Explorer, *Space Sci. Rev.*, *86*, 563, doi:10.1007/978-94-011-4762-0_20.

Milan, S. E., M. Lester, S. W. H. Cowley, J. Moen, P. E. Sandholt, and C. J. Owen (1999), Meridian-scanning photometer, coherent HF radar, and magnetometer observations of the cusp: A case study, *Ann. Geophys.*, *17*(2), 159–172, doi:10.1007/s00585-999-0159-5.

Milan, S. E., M. Lester, S. W. H. Cowley, and M. Brittnacher (2000), Convection and auroral response to a southward turning of the IMF: Polar UVI, CUTLASS, and IMAGE signatures of transient magnetic flux transfer at the magnetopause, *J. Geophys. Res.*, *105*(A7), 15,741–15,756, doi:10.1029/2000JA900022.

Moen, J., P. Sandholt, M. Lockwood, W. Denig, U. Løvhaug, B. Lybekk, A. Egeland, D. Opsvik, and E. Friis-Christensen (1995), Events of enhanced convection and related dayside auroral activity, *J. Geophys. Res.*, *100*(A12), 23,917–23,934, doi:10.1029/95JA02585.

Moen, J., D. Evans, H. C. Carlson, and M. Lockwood (1996), Dayside moving auroral transients related to LLBL dynamics, *Geophys. Res. Lett.*, *23*(22), 3247–3250, doi:10.1029/96GL02766.

Moen, J., D. A. Lorentzen, and F. Sigernes (1998), Dayside moving auroral forms and bursty proton auroral events in relation to particle boundaries observed by NOAA 12, *J. Geophys. Res.*, *103*(A7), 14,855–14,863, doi:10.1029/97JA02877.

Moen, J., H. C. Carlson, S. E. Milan, N. Shumilov, B. Lybekk, P. E. Sandholt, and M. Lester (2001), On the collocation between dayside auroral activity and coherent HF radar backscatter, *Ann. Geophys.*, *18*(12), 1531–1549, doi:10.1007/s00585-001-1531-2.

Moen, J., I. K. Walker, L. Kersley, and S. E. Milan (2002), On the generation of cusp HF backscatter irregularities, *J. Geophys. Res.*, *107*(A4), 1044, doi:10.1029/2001JA000111.

Moen, J., H. C. Carlson, K. Oksavik, C. P. Nielsen, S. E. Pryse, H. R. Middleton, I. W. McCrea, and P. Gallop (2006), EISCAT observations of plasma patches at sub-auroral cusp latitudes, *Ann. Geophys.*, *24*(9), 2363–2374, doi:10.5194/angeo-24-2363-2006.

Moen, J., Y. Rinne, H. C. Carlson, K. Oksavik, R. Fujii, and H. Opgenoorth (2008), On the relationship between thin Birkeland current arcs and reversed flow channels in the winter cusp/cleft ionosphere, *J. Geophys. Res.*, *113*, A09220, doi:10.1029/2008JA013061.

Moen, J., K. Oksavik, L. Alfonsi, Y. Daabakk, V. Romano, and L. Spogli (2013), Space weather challenges of the polar cap ionosphere, *J. Space Weather Space Clim.*, *3*, A02, doi:10.1051/swsc/2013025.

Newell, P. T., and C. I. Meng (1995), Cusp low-energy ion cutoffs: A survey and implications for merging, *J. Geophys. Res.*, *100*(A11), 21,943–21,951, doi:10.1029/95JA01608.

Newell, P. T., and C.-I. Meng (1991), Ion acceleration at the equatorward edge of the cusp: Low altitude observations of patchy merging, *Geophys. Res. Lett.*, *18*(10), 1829–1832, doi:10.1029/91GL02088.

Newell, P. T., and C.-I. Meng (1998), Open and closed low latitude boundary layer, in *Polar Cap Boundary Phenomena*, edited by J. Moen et al., 91 pp., Kluwer Acad., Norwell, Mass.

Newell, P. T., W. J. Burke, E. R. Sánchez, C.-I. Meng, M. E. Greenspan, and C. R. Clauer (1991), The low-latitude boundary layer and the boundary plasma sheet at low altitude: Prenoon precipitation regions and convection reversal boundaries, *J. Geophys. Res.*, *96*(A12), 21013, doi:10.1029/91JA01818.

Ni, B., R. M. Thorne, R. B. Horne, N. P. Meredith, Y. Y. Shprits, L. Chen, and W. Li (2011a), Resonant scattering of plasma sheet electrons leading to diffuse auroral precipitation: 1. Evaluation for electrostatic electron cyclotron harmonic waves, *J. Geophys. Res.*, *116*, A04218, doi:10.1029/2010JA016232.

Ni, B., R. M. Thorne, N. P. Meredith, R. B. Horne, and Y. Y. Shprits (2011b), Resonant scattering of plasma sheet electrons leading to diffuse auroral precipitation: 2. Evaluation for whistler mode chorus waves, *J. Geophys. Res.*, *116*, A04219, doi:10.1029/2010JA016233.

Nishida, A., T. Mukai, H. Hayakawa, A. Matsuoka, K. Tsuruda, N. Kaya, and H. Fukunishi (1993), Unexpected features of the ion precipitation in the so-called cleft/low-latitude boundary layer region: Association with sunward convection and occurrence on open field lines, *J. Geophys. Res.*, *98*(A7), 11,161–11,176, doi:10.1029/92JA00516.

Nishimura, Y., et al. (2013), Structures of dayside whistler-mode waves deduced from conjugate diffuse aurora, *J. Geophys. Res. Space Physics*, *118*, 664–673, doi:10.1029/2012JA018242.

Øieroset, M., T. D. Phan, V. Angelopoulos, J. P. Eastwood, J. McFadden, D. Larson, C. W. Carlson, K. H. Glassmeier, M. Fujimoto, and J. Raeder (2008), THEMIS multi-spacecraft observations of magnetosheath plasma penetration deep into the dayside low-latitude magnetosphere for northward and strong B$_y$ IMF, *Geophys. Res. Lett.*, *35*, L17S11, doi:10.1029/2008GL033661.

Oksavik, K., J. Moen, and H. C. Carlson (2004a), High-resolution observations of the small-scale flow pattern associated with a poleward moving auroral form in the cusp, *Geophys. Res. Lett.*, *31*, L11807, doi:10.1029/2004GL019838.

Oksavik, K., F. Søraas, J. Moen, R. Pfaff, J. A. Davies, and M. Lester (2004b), Simultaneous optical, CUTLASS HF radar, and FAST spacecraft observations: Signatures of boundary layer processes in the cusp, *Ann. Geophys.*, *22*(2), 511–525, doi:10.5194/angeo-22-511-2004.

Oksavik, K., J. M. Ruohoniemi, R. A. Greenwald, J. B. H. Baker, J. Moen, H. C. Carlson, T. K. Yeoman, and M. Lester (2006), Observations of isolated polar cap patches by the European Incoherent Scatter (EISCAT) Svalbard and Super Dual Auroral Radar Network (SuperDARN) Finland radars, *J. Geophys. Res.*, *111*, A05310, doi:10.1029/2005JA011400.

Oksavik, K., V. L. Barth, J. Moen, and M. Lester (2010), On the entry and transit of high-density plasma across the polar cap, *J. Geophys. Res.*, *115*, A12308, doi:10.1029/2010JA015817.

Oksavik, K., C. van der Meeren, D. A. Lorentzen, L. J. Baddeley, and J. Moen (2015), Scintillation and loss of signal lock from poleward moving auroral forms in the cusp ionosphere, *J. Geophys. Res. Space Physics*, *120*, 9161–9175, doi:10.1002/2015JA021528.

Onsager, T., and M. Lockwood (1997), High-latitude particle precipitation and its relationship to magnetospheric source regions, *Space Sci. Rev.*, *80*(1–2), 77–107, doi:10.1023/A:1004925720793.

Pinnock, M., A. S. Rodger, J. R. Dudeney, F. Rich, and K. B. Baker (1995), High spatial and temporal resolution observations of the ionospheric cusp, *Ann. Geophys.*, *13*(9), 919–925, doi:10.1007/s00585-995-0919-9.

Rinne, Y., J. Moen, K. Oksavik, and H. C. Carlson (2007), Reversed flow events in the winter cusp ionosphere observed by the European Incoherent Scatter (EISCAT) Svalbard radar, *J. Geophys. Res.*, *112*, A10313, doi:10.1029/2007JA012366.

Rodger, A. S., and M. Pinnock (1997), The ionospheric response to flux transfer events: The first few minutes, *Ann. Geophys.*, *15*(6), 685–691, doi:10.1007/s00585-997-0685-y.

Rodger, A. S., S. B. Mende, T. J. Rosenberg, and K. B. Baker (1995), Simultaneous optical and HF radar observations of the ionospheric cusp, *Geophys. Res. Lett.*, *22*(15), 2045–2048, doi:10.1029/95GL01797.

Ruohoniemi, J. M., and K. B. Baker (1998), Large-scale imaging of high-latitude convection with Super Dual Auroral Radar Network HF radar observations, *J. Geophys. Res.*, *103*(A9), 20,797–20,811, doi:10.1029/98JA01288.

Sandholt, P. E., and C. J. Farrugia (2007), Role of poleward moving auroral forms in the dawn-dusk auroral precipitation asymmetries induced by IMF By, *J. Geophys. Res.*, *112*, A04203, doi:10.1029/2006JA011952.

Sandholt, P. E., and P. T. Newell (1992), Ground and satellite observations of an auroral event at the cusp/cleft equatorward boundary, *J. Geophys. Res.*, *97*(A6), 8685–8691, doi:10.1029/91JA02995.

Sandholt, P. E., C. S. Deehr, A. Egeland, B. Lybekk, R. Viereck, and G. J. Romick (1986), Signatures in the dayside aurora of plasma transfer from the magnetosheath, *J. Geophys. Res.*, *91*(A9), 10,063–10,079, doi:10.1029/JA091iA09p10063.

Sandholt, P. E., C. J. Farrugia, J. Moen, Ø. Noraberg, B. Lybekk, T. Sten, and T. Hansen (1998), A classification of dayside auroral forms and activities as a function of interplanetary magnetic field orientation, *J. Geophys. Res.*, *103*(A10), 23,325–23,345, doi:10.1029/98JA02156.

Sandholt, P. E., C. J. Farrugia, S. W. H. Cowley, and M. Lester (2001), Dayside auroral bifurcation sequence during By-dominated interplanetary magnetic field: Relationship with merging and lobe convection cells, *J. Geophys. Res.*, *106*(A8), 15,429–15,444, doi:10.1029/2000JA900161.

Sandholt, P. E., W. F. Denig, C. J. Farrugia, B. Lybekk, and E. Trondsen (2002), Auroral structure at the cusp equatorward boundary: Relationship with the electron edge of low-latitude boundary layer precipitation, *J. Geophys. Res.*, *107*(A9), 1235, doi:10.1029/2001JA005081.

Shi, Q. Q., et al. (2009), Cluster observations of the entry layer equatorward of the cusp under northward interplanetary magnetic field, *J. Geophys. Res.*, *114*, A12219, doi:10.1029/2009JA014475.

Shi, Q. Q., et al. (2013), Solar wind entry into the high-latitude terrestrial magnetosphere during geomagnetically quiet times, *Nat. Commun.*, *4*, 1466, doi:10.1038/ncomms2476.

Smith, C. W., J. L'Heureux, N. F. Ness, M. H. Acuña, L. F. Burlaga, and J. Scheifele (1998), The ACE magnetic fields experiment, *Space Sci. Rev.*, *86*, 613, doi:10.1007/978-94-011-4762-0_21.

Southwood, D. J. (1987), The ionospheric signature of flux transfer events, *J. Geophys. Res.*, *92*(A4), 3207–3213, doi:10.1029/JA092iA04p03207.

Thorne, R. M., B. Ni, X. Tao, R. B. Horne, and N. P. Meredith (2010), Scattering by chorus waves as the dominant cause of diffuse auroral precipitation, *Nature*, *467*(7318), 943–946, doi:10.1038/nature09467.

Thorolfsson, A., J.-C. Cerisier, M. Lockwood, P. Sandholt, C. Senior, and M. Lester (2000), Simultaneous optical and radar signatures of poleward-moving auroral forms, *Ann. Geophys.*, *18*(9), 1054–1066, doi:10.1007/s00585-000-1054-2.

Tsurutani, B. T., A. L. Brinca, E. J. Smith, R. T. Okida, R. R. Anderson, and T. E. Eastman (1989), A statistical study of ELF-VLF plasma waves at the magnetopause, *J. Geophys. Res.*, *94*(A2), 1270–1280, doi:10.1029/JA094iA02p01270.

Walsh, B., J. Foster, P. Erickson, and D. Sibeck (2014), Simultaneous ground-and space-based observations of the plasmaspheric plume and reconnection, *Science*, *343*(6175), 1122–1125, doi:10.1126/science.1247212.

Wing, S., P. T. Newell, and J. M. Ruohoniemi (2001), Double cusp: Model prediction and observational verification, *J. Geophys. Res.*, *106*(A11), 25,571–25,593, doi:10.1029/2000JA000402.

Yeoman, T. K., M. Lester, S. W. H. Cowley, S. E. Milan, J. Moen, and P. E. Sandholt (1997), Simultaneous observations of the cusp in optical, DMSP and HF radar data, *Geophys. Res. Lett.*, *24*(17), 2251–2254, doi:10.1029/97GL02072.

Yeoman, T. K., G. Chisham, L. J. Baddeley, R. S. Dhillon, T. J. T. Karhunen, T. R. Robinson, A. Senior, and D. M. Wright (2008), Mapping ionospheric backscatter measured by the SuperDARN HF radars—Part 2: Assessing SuperDARN virtual height models, *Ann. Geophys.*, *26*(4), 843–852, doi:10.5194/angeo-26-843-2008.

Zhang, Q. H., et al. (2011), On the importance of interplanetary magnetic field |By| on polar cap patch formation, *J. Geophys. Res.*, *116*, A05308, doi:10.1029/2010JA016287.

Zhang, Q. H., et al. (2013), Direct observations of the evolution of polar cap ionization patches, *Science*, *339*(6127), 1597–1600, doi:10.1126/science.1231487.